Flexible and Printed Electronics

Pattern-dependent resistivity variations in inkjet-printed conductors due to non-uniform ink drying

IOP Publishing Flex. Print. Electron. 9 (2024) 015011 https://doi.org/10.1088/2058-8585/ad3115

Flexible and Printed Electronics

OPEN ACCESS

RECEIVED
10 July 2023

REVISED
11 December 2023

ACCEPTED FOR PUBLICATION
7 March 2024

PUBLISHED
20 March 2024

PAPER

Pattern-dependent resistivity variations in inkjet-printed conductors due to non-uniform ink drying

Milad Ghalamboran*, Mohammad Nazeri and Gerd Grau

Department of Electrical Engineering and Computer Science, Lassonde School of Engineering, York University, 4700 Keele Street, Toronto, ON M3J 1P3, Canada

* Author to whom any correspondence should be addressed.

E-mail: miladghn@yorku.ca

Keywords: printed electronics, inkjet printing, intense pulsed light (IPL) sintering, silver nanoparticle ink, resistivity variation

Supplementary material for this article is available online

Abstract

When fabricating inkjet-printed electronic devices and circuits, inkjet-printed conductive materials require drying and sintering to improve electrical conductivity. Electrical conductivity should be the same irrespective of pattern design, size, location, or density of adjacent patterns. However, we demonstrate that spatial variations in the drying process for inkjet-printed patterns with proximity to others cause resistivity variations. These resistivity variations are studied here experimentally for different circuit patterns and in arrays of inkjet-printed square electrodes. This variation depends not only on the location of each electrode in an array but also on the number of electrodes. This means that for the same drying temperature and duration, the array with a larger number of electrodes exhibits a larger resistivity variation. The sooner an electrode dries, the lower resistivity it achieves. The resistivity variation between an individual electrode and the center electrode in a 7×7 electrode array can be a factor of seven. This variation decreases for lower numbers of electrodes to a factor of three for a 3×3 array. Furthermore, x-ray photoelectron spectroscopy analyses provide evidence for the residual presence of carbon-based materials within electrodes after the drying process. These results confirm that the location of electrodes within an array significantly influences the amount of residual carbon-based materials, thereby contributing to resistivity variations. Although intense pulsed light sintering can decrease this variation, its optimal parameters depend on the printed designs, and our simulation results show a non-uniform temperature profile over the electrode arrays. Temperature increases more at the center of patterns than the corners, which can be useful in this case to improve resistivity uniformity. In this study, for the first time, we show how different printed shapes and designs can result in non-uniform resistivity after drying and sintering.

1. Introduction

Printed electronics can produce various electronic thin-film devices, including diodes [1, 2], capacitors [3], resistors [4, 5], solar cells [6, 7], sensors [8, 9], batteries [10], antennas [11, 12], and transistors [13–15]. Some advantages of printing methods are the possibility of printing over large areas, cost reduction, and rapid manufacturing [16, 17]. Another advantage of this technique for the fabrication of wearable and flexible electronics is the use of biodegradable and recyclable materials. For example, without the need for etching and lithography masks, additive manufacturing and printed electronics as a fabrication method reduce the number of materials in a fabrication line [16, 17]. This feature also helps to cut down on fabrication costs. Furthermore, circuits and electrical devices may be printed on various surfaces using functional inks, unlike traditional graphics arts printing that is limited to pictorial patterns [18–20]. Conductive inks [21] are particularly important as almost all electronic devices and systems require

electrodes or other metallic structures. The quality factor (Q) of an inductor is influenced by its resistance as shown in equation (1), where R is DC resistance, and ωL is the inductive reactance

$$\mathrm{Q} = \frac{\omega L}{R}. \quad (1)$$

The most popular inks for printing electrically conductive connections in printed electronics, especially wearable electronics, are metal inks [22–24]. Metal nanoparticles or precursors may be dispersed in water or organic solvents [25–27], and various stabilizers are added to the inks to ensure proper stability and prevent agglomeration or condensation. Gold (Au) is recognized as an ink with the highest electrical conductivity among metal inks. However, it is not frequently used due to economic reasons. Silver (Ag) offers almost the same qualities at a lower cost [28]. Copper (Cu) nanoparticles have been used as a less expensive substitute for silver inks. However, they have a stronger tendency to oxidize in the presence of air [29]. Conductive polymers have also recently been explored as a result of their desirable qualities, such as low weight, flexibility, cost-effectiveness, bio-compatibility, and ease of production. However, there are some drawbacks to using conductive polymers, such as lower electrical conductivity compared to metal inks and carbon-based inks [30], low concentration of polymer inks that results in long drying times, and also limitations in terms of stability and processability [31].

After the ink is printed, solvents need to be removed from the ink and vaporized. The remaining ink components form a solid film when the liquid phase evaporates. As the ink begins to dry, the viscosity will increase, decreasing the evaporation speed. In addition, the ligands and binders that encapsulate the nanoparticles to suspend them in solution limit the electrical conductivity of the printed thin-film pattern. These components should be decomposed during the sintering process. This process not only deteriorates the organic components but also fuses the nanoparticles, improving the printed pattern's electrical conductivity [32, 33]. Achieving uniform evaporation in inkjet-printed electronics poses challenges, including the coffee-ring effect leading to non-uniform thickness. This complexity, extending beyond traditional inks, involves anchored liquid points during evaporation, as detailed by Deegan *et al* [34]. Capillary flow, explained by Deegan's work, propels particles towards outer boundaries. Fischer's [35] model highlights convective currents transporting solute to the droplet's outer rim. Marangoni effects influence fluid movements near edges. These reports focus on the effect of non-uniform drying on fluid flow and thickness non-uniformities within printed features. Here, we report the effect of non-uniform drying on the material properties of inkjet-printed nanoparticle conductors, namely resistivity. The effect of non-uniform sintering of nanoparticles has been studied for different sintering methods such as laser sintering for rapid ink metallization or plasma sintering. Swift metallization results from fast evaporation of volatile constituents, forming a dense surface layer and causing defects. This accelerated surface sintering hinders complete sintering toward the ink/substrate interface, leading to poor adhesion post-sintering [36]. In these reports, non-uniform sintering in the film thickness dimension is studied. Here, we study the non-uniform evaporation and sintering in the lateral pattern dimension leading to different resistivity values in different parts of a circuit.

There are several sintering techniques for improving the electrical conductivity of metal nanoparticle films. The most common is thermal sintering, carried out on a hot plate or in an oven, potentially in a reducing atmosphere for metals such as copper. Nanoparticles have a high surface-to-volume ratio, and the self-diffusion of metal nanoparticles is faster than for bulk metal, which causes a lower melting point for metal nanoparticles. Therefore, a temperature around 80 °C–200 °C can remove the organic components of the ink, and sinter the nanoparticles [37]. Thermal sintering has two main drawbacks: first, it can deform low-cost flexible plastic substrates, and second, it can be time-consuming, especially for roll-to-roll printing.

Conversely, photonic sintering methods allow the sintering of nanoparticles on sensitive substrates [38, 39]. Among them, intense pulsed light (IPL) sintering using a xenon flash lamp is attractive for sintering metal nanoparticles. When Kinney and colleagues published their historical patent in 1969, they started using the IPL technique for sintering nanoparticles, which is now applied to printed materials for electronic devices [40]. The thin film of metal nanoparticles will absorb the millisecond pulsed light and quickly cool down without heating the substrate, making it possible to do so without damaging the heat-sensitive polymer. Additionally, the IPL sintering method is fast, speeding up the production process by increasing temperature within milliseconds [41].

Many studies of IPL sintering have been performed for uniform designs such as blanket films or individual lines, which means that the heat energy distribution is uniform, and the resistivity of the printed pattern can be uniform. However, to form different electronic devices and circuits, such as sensors, micro-heaters, wireless power transfer and antennas [42–44], different-sized patterns must be printed on a substrate that may include more complicated patterns, for example, spirals, interdigitated lines, or closely spaced electrodes in contrast to simple shapes such as circles, rectangles, or squares. These printed patterns also require a sintering process. A study by Kim *et al* discovered that IPL sintering characteristics

depend on the distance between adjacent printed patterns and the size of them because wider lines absorb more heat, which can spread more easily across the smaller gaps. When this happens with complex patterns, it can be hard to achieve the same resistance everywhere within the pattern [45]. Another process that can potentially lead to resistance variations when patterns are printed with small gap distances is the drying step. A study compared evaporation of a single water droplet and a droplet surrounded by six other droplets. The time of drying for single water droplet is five times less than the droplet surrounded by six droplets because the relative humidity saturates the air around the center drop due to the evaporation of neighboring drops. However, the effect of this phenomenon on drying inks containing functional materials was not studied [46].

Here in this paper, we show that electrical resistivity of printed metal nanoparticle conductors strongly depends on the pattern design due to the drying and subsequent sintering. This is important in systems with multiple different types of patterns as illustrated in figure 1(a). For example, a dense antenna pattern will dry more slowly than a sparse pattern such as resistive sensor leading to different resistivities. Conversely, subsequent IPL sintering can improve the resistivity uniformity. Here, we demonstrate that these two interlinked phenomena significantly affect the resistance of several inkjet-printed patterns used in printed devices and circuits and should be taken into account by circuit designers. The effects are studied systematically using arrays of printed electrodes with small gap distances. The term 'variations' in this study refers to the differences in resistivity observed between different patterns and different locations within larger patterns, specifically how the resistivity of printed conductors varies depending on their geometric design.

2. Results and discussion

The pattern-dependent drying and sintering effects are studied here by printing various line patterns with different geometries, including square wave shapes, large U shapes, straight lines, small U shapes, and spirals (refer to figure 1(a)). These line patterns share the same length and width but exhibit varying local densities and numbers of corners. During the drying step, the solvent's vapor density is higher around patterns characterized by increased local pattern density. In contrast, during the subsequent sintering step, we observed higher temperature rises. This elevated temperature leads to a more substantial reduction in resistance, contributing to a higher resistance reduction factor compared to patterns with lower local density geometries, as depicted in figure 1(b).

The printed patterns are dried at 60 °C for 25 min and IPL sintered with 15 J cm^{-2}. All the shapes are printed with the same total amount of silver ink, which is 1288 drops, and the same linewidth. By controlling the total amount of silver ink (1288 drops) and maintaining the same linewidth, we ensured that variations in ink quantity per unit length and trace thickness as well as overall trace length were not contributing factors to the observed resistance differences between different shapes. The only difference between the patterns is the number of corners and the local density of the pattern. To calculate resistivity from resistance measurements for the different patterns, microscope images of the printed patterns were imported into COMSOL Multiphysics with the average thickness of each pattern obtained from profilometry, and the current and voltage distributions were calculated. The results show a clear trend of increasing resistivity after drying with increasing pattern density in figure 1(b). The spiral design with the closest printed features, i.e. adjacent lines, shows the highest resistivity after drying compared to other shapes (57% larger than the line shape with the lowest density). The large U shape and small U shape are two examples of the same fundamental shape to study the effect of pattern density. The smaller U shape shows a higher resistivity after drying compared to the large U shape (26.8% higher). After IPL sintering, the spiral design with the highest local pattern density shows the highest resistivity reduction by a factor of 2.47 but its resistivity after sintering is still 29.4% times larger than the line shape. These experiments show that drying is dependent on the pattern geometry and compact designs with small gap distances dry more slowly than less dense designs resulting in a higher resistivity for the same drying time. Conversely, after IPL sintering, compact designs with small gap distances show a larger resistivity reduction factor than less dense designs due to the more concentrated temperature distribution over the designs with denser local pattern density.

To study these phenomena more systematically, square-shaped electrodes with different pattern densities are inkjet printed, shown schematically in figure 2(a). The electrodes are printed as an individual, and arrays of 9 (3 × 3), 25 (5 × 5), and 49 (7 × 7) square electrodes. Square array patterns were chosen as our experimental platform for several reasons. They offer a controlled and standardized environment, allowing systematic variation of square location and density while keeping other factors constant. This controlled setup is crucial for isolating pattern-dependent variables, such as drying and sintering. Furthermore, square arrays are versatile and adaptable for studying a wide range of patterns, making them a suitable model for establishing fundamental principles that can be applied to more complex designs commonly encountered in printed electronics. Additionally, square arrays facilitate the clear presentation of our findings and enhance accessibility to a broader audience. In essence, the use of square arrays enables us to systematically investigate

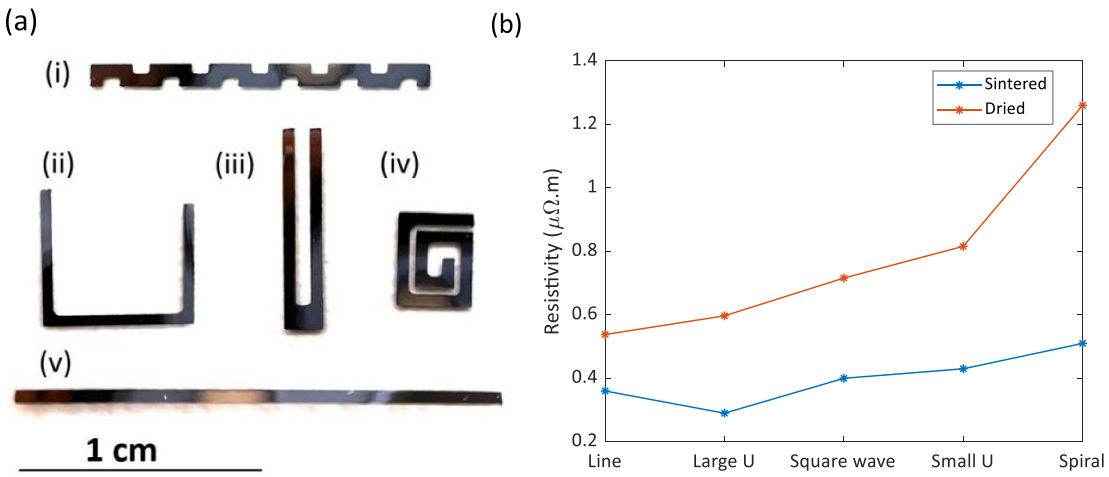

Figure 1. (a) Different pattern geometries that were studied after drying and sintering: (i) square wave, (ii) large U shape, (iii) small U shape, (iv) spiral pattern, and (v) straight line. (b) Resistivity of these patterns after drying and sintering, which shows an increasing trend from line to spiral pattern.

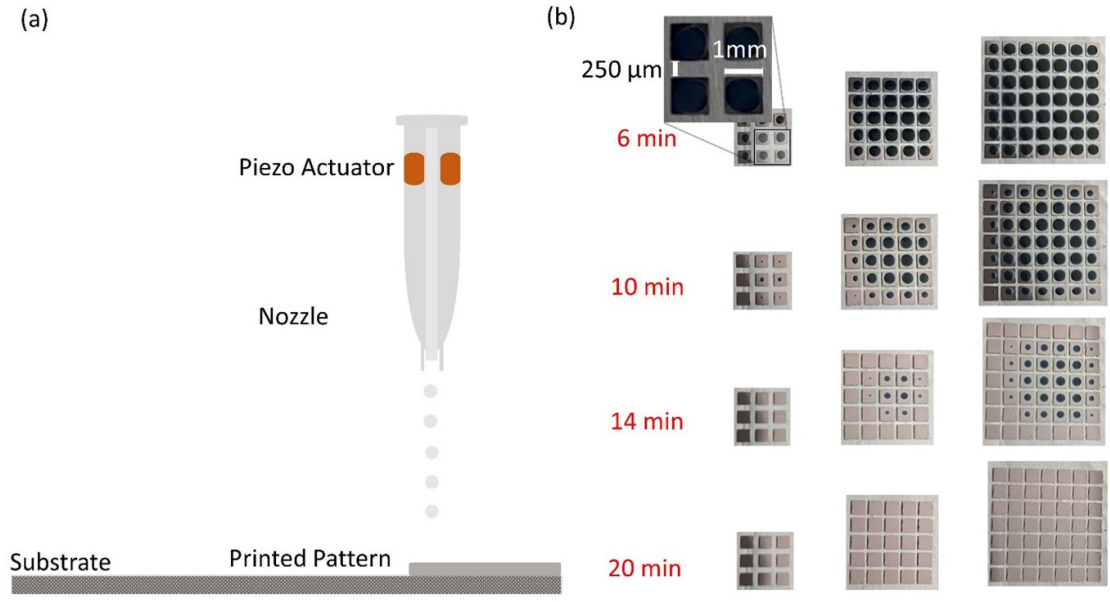

Figure 2. (a) Schematic of inkjet printer, (b) drying pattern of three different electrode arrays at four different times.

the fundamental effects of non-uniform drying and IPL sintering on resistivity in different locations, laying a robust foundation for understanding pattern-dependent resistivity variations in printed conductors that can be extrapolated to other practical applications. Moreover, an individual electrode was printed far away from the array to study its resistivity as a reference electrode. The individual electrode dried first, then the corners of arrays and finally the center electrode in the array. The drying pattern of the printed designs with gap distance of 250 μm is shown in figure 2(b) at four different times on a hot plate at 60 °C. The thickness of the square shape electrodes is 500 $\pm$ 60 nm and the average thickness of complex designs is 750 $\pm$ 70 nm. The thickness is controlled through a variable drop spacing method, which enhances both the sharpness of the edges and the uniformity of thickness (shown in figure S1). In a 3 $\times$ 3 electrode array after 10 min the corners will be dried, while the 5 $\times$ 5 and 7 $\times$ 7 arrays are still completely wet. The 7 $\times$ 7 array needs more drying time than 3 $\times$ 3 and 5 $\times$ 5; even after 14 min, the 7 $\times$ 7 array has many wet electrodes when most of the electrodes are dried completely in the 5 $\times$ 5 array. Here, the 7 $\times$ 7 array with 250 μm gap is dried after 20 min and this drying time is used for all other electrode arrays with smaller size or larger gaps. For 100 μm gap distance between electrodes, this time is increased to 30 min.

The average resistivity of electrodes with different distances from the center electrode is measured

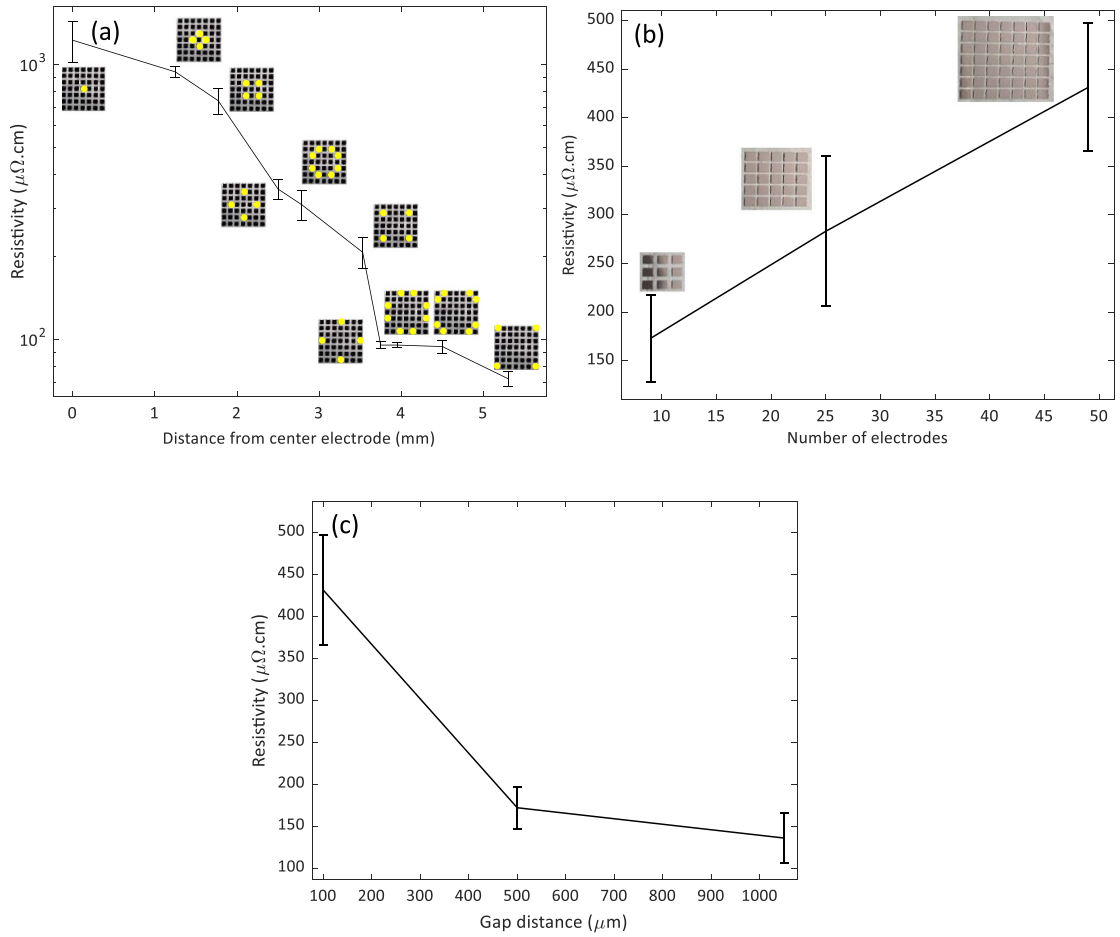

Figure 3. (a) Resistivity versus distance from the center electrode for 7 × 7 electrode array with 250 μm gap distance after drying for 20 min at 60 °C. (b) Resistivity variation for center electrodes in 3 × 3, 5 × 5, and 7 × 7 electrode arrays all with 100 μm gap distance after drying at 60 °C for 30 min on a hot plate. (c) Resistivity variation for center electrodes in 7 × 7 electrode arrays with three different gap distances after drying at 60 °C for 30 min on a hot plate. (The error bar represents standard deviation).

after drying on a hot plate at 60 °C for 20 min using the van der Pauw (VDP) method. The results for a 7 × 7 array with 250 μm gap distance are shown in figure 3(a). There is a descending trend of resistivity from the center to the corner electrodes, which follows the drying pattern shown in figure 2(b). The sooner the electrode dries, the lower resistivity it achieves. The center electrode shows a resistivity (1433 ± 208 $\mu\Omega$.cm) 21 times larger than individual electrodes (66.19 ± 4.27 $\mu\Omega$.cm) and 19 times larger than corner electrodes (71.99 ± 4.33 $\mu\Omega$.cm).

In order to study the resistivity variation for electrode arrays with different numbers of electrodes, 3 × 3 and 5 × 5 arrays were also studied with a gap distance of 100 μm and 30 min drying on a hot plate. The resistivity of the center electrodes is shown in figure 3(b). This experiment demonstrates that the resistivity of electrodes in an array depends on the overall density of electrodes in the array, where the center electrode in a 3 × 3 array shows smaller resistivity than center electrodes in 5 × 5 and 7 × 7 arrays. Also, the same drying condition were applied to 7 × 7 arrays with three different gap distances and the results are shown in figure 3(c). Increasing gap distance increases evaporation rate, which causes lower resistivity for the center electrodes.

During drying, both the number of electrodes and the gap distance between them affect the vapor density of the ink's solvent. Increasing the number of electrodes and decreasing the gap distance increases the vapor density in the center of an array, which decreases the evaporation rate, and this can cause a delay in the drying of the center electrode. In order to show the vapor density effect on drying time and uniformity, drying of a 7 × 7 electrode array was performed in an atmosphere saturated with the ink's solvent triethylene glycol monoethyl ether (TGME). Drying time was increased from 30 min to 45 min and resistivity variation from corner to center electrodes was decreased to 25.15% compared to normal drying under atmospheric conditions (439.80%).

In order to study the generality of this phenomenon, resistivity variations after drying were studied with another ink that contains Cu nanoparticles. A 7 × 7 electrode array was printed and dried in a vacuum oven at 60 °C. After 30 min the corner and center electrodes show a resistivity

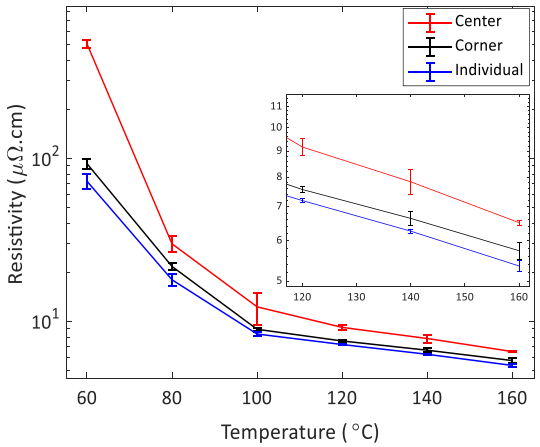

Figure 4. Resistivity of individual, corner, and center electrodes in a 7 × 7 array with a gap distance of 100 μm after sintering at different temperatures from 60 °C to 160 °C for 30 min. (The error bar represents standard deviation).

of 49.4 ± 3.96 $\mu\Omega$.cm and 109.38 ± 2.57 $\mu\Omega$.cm, respectively. This shows that the non-uniform drying and resistivity variation phenomena are not limited to one ink.

After drying, sintering treatment is necessary for printed silver nanoparticles to improve overall resistivity of electrodes. Here, two different sintering methods are applied: conventional thermal sintering on a hot plate and IPL sintering as a photonic method. The electrical resistivity of a 7 × 7 electrode array with a gap distance of 100 μm is studied using a hot plate at different temperatures (60 °C–160 °C) with a sintering time of 30 min. The resistivity of three different electrode locations (individual, corner, and center electrodes) after thermal sintering are shown in figure 4. It shows an improvement in electrical resistivity of all electrodes with increasing sintering temperature and also less variation from center to corners compared to before sintering. After sintering at 160 °C, a 17% resistivity variation remains between center and corner and 27% between individual and center.

IPL sintering is applied to all arrays (3 × 3, 5 × 5, and 7 × 7) with the same gap distance (100 μm) with different numbers of pulses and energy densities. During IPL sintering, the voltage is kept constant at 2500 V for a range of 5–150 pulses. However, after 150 pulses, the resistivity no longer changes. To continue the sintering process, the voltage is increased to 3000 V and 180 pulses are applied to the electrodes. The resistivity of the individual electrode is shown separately in figure 5(a), and all the results for arrays are shown in figures 5(b)–(d). The resistivity of as dried individual electrodes reduces 22 times after initial sintering at 22.5 J cm^{-2} (from 66.19 ± 4.27 $\mu\Omega$.cm to 2.99 ± 1.69 $\mu\Omega$.cm), while it is 16 times for corner (79.89 ± 3.57 $\mu\Omega$.cm to 4.99 ± 0.48 $\mu\Omega$.cm) and 65 times for center electrodes (431.25 ± 65.75–6.61 ± 0.62 $\mu\Omega$.cm) in a 7 × 7 array. Increasing energy density to 1020 J cm^{-2} improves the resistivity to 1.85 ± 0.05 $\mu\Omega$.cm, 2.05 ± 0.09 $\mu\Omega$.cm, and 2.16 ± 0.06 $\mu\Omega$.cm for individual, corner and center electrodes, respectively. With increasing number of electrodes, the variation in resistivity from the corner to center electrodes increases after drying. After sintering at 22.5 J cm^{-2}, corner and center of electrodes in an array with a large number of electrodes still show a higher resistivity than smaller arrays. The resistivity after IPL at 1020 J cm^{-2} does not depend on array size. The resistivity of the center electrode in 3 × 3, 5 × 5, and 7 × 7 arrays is decreased by a factor of 82.12, 136.17, and 199.65 respectively after sintering at 1020 J cm^{-2}, which is the best energy density for the lowest variation (less than 6%) between corner and center as well as the lowest resistivity overall. Conversely, the lowest variation after thermal sintering at 160 °C for 30 min on a hot plate is still 17%.

Oversintering of electrodes after applying pulses with 1224 J cm^2 causes a resistivity increase for all electrode arrays and is therefore the limit for increasing the energy density. The SEM images in figure 5 show sintered nanoparticles in a corner electrode in a 7 × 7 array with a gap distance of 100 μm. After sintering at 1020 J cm^2, the image (figure 5(e)) shows a continuous and even silver surface, but after oversintering at 1224 J cm^2 some holes can be seen in figure 5(f), which increases the resistivity.

As discussed for the drying step, another parameter for controlling the resistivity variation in electrode arrays is the gap distance between the printed electrodes. Three different gap distances are studied for a 7 × 7 electrode array, and the resistivity of electrodes are normalized to the individual electrode as shown in figure 6. Figure 6(a) shows a descending trend for resistivity with increasing gap distance after drying. The resistivity of the center electrode is 6.7 and 5.4 times larger than the individual and corner electrodes, respectively, with a gap distance of 100 μm. This decreases to 1.7 and 1.6 times for a gap distance of 1050 μm. After IPL sintering with an energy density of 540 J cm^{-2}, the difference in resistivity of center electrodes between different gap distances decreases significantly (shown in figure 6(b)). The difference becomes 8.3% from 100 μm to 500 μm gap distance, and 17% from 100 μm to 1050 μm (shown in figure 6(b)). As mentioned previously, after sintering at 1020 J cm^{-2}, overall resistivity is minimized, corners and center have the lowest variation, and the difference between different gap distances is the lowest value as shown in figure 6(c). After 1224 J cm^{-2}, the descending trend with increasing gap distance becomes stronger again and all resistivity values are increased (figure 6(d)). This means that for a lower gap distance such as 100 μm, oversintering causes a larger resistivity, while for a larger

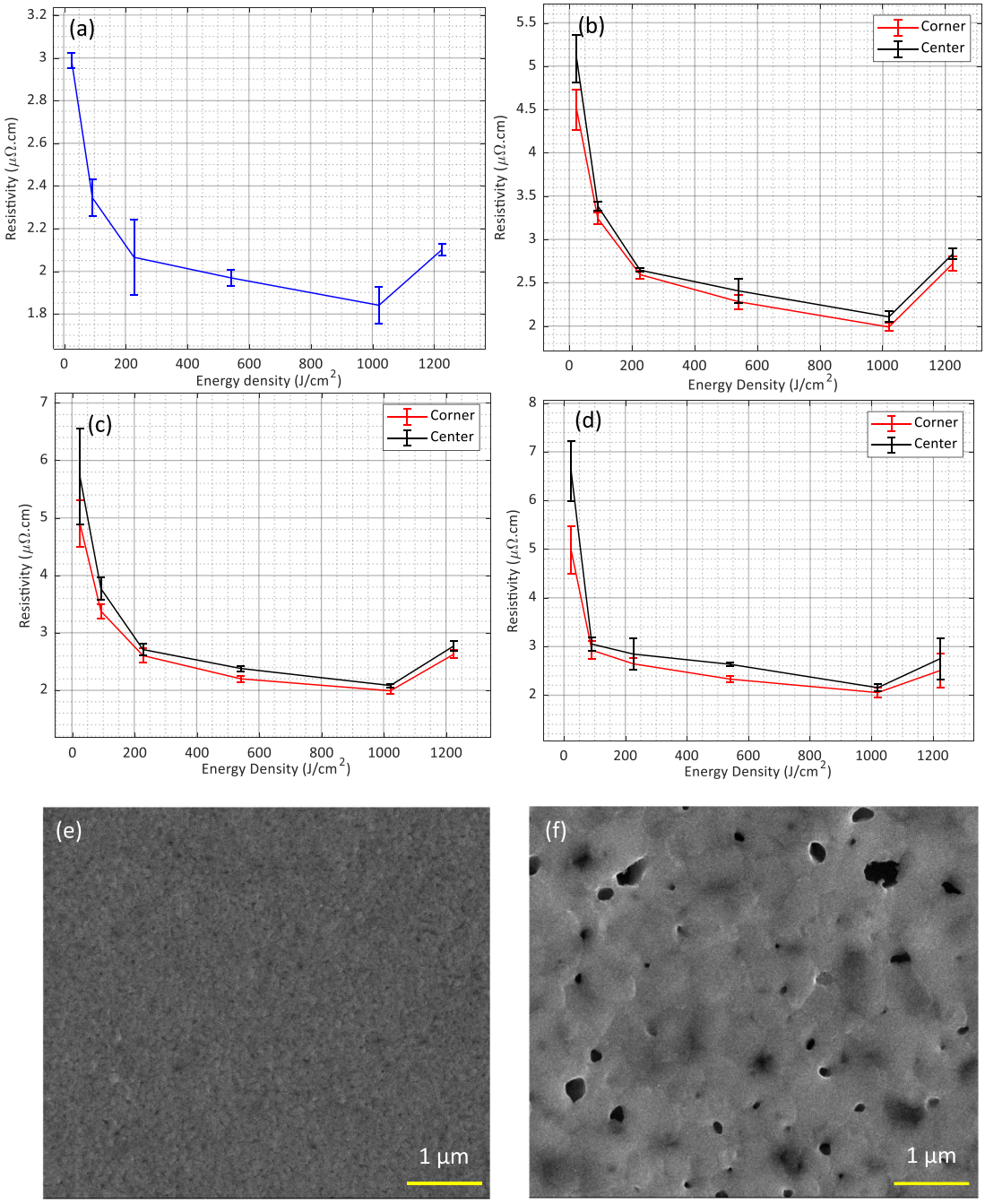

Figure 5. Change in resistivity as a function of energy density for (a) individual electrode, and corners and centers of (b) 3 × 3, (c) 5 × 5, and (d) 7 × 7 arrays. Note, the *y*-axis scales are different in these graphs as larger arrays generally exhibit larger resistivity. SEM images of corner electrode after sintering at (e) 1020 J cm^{-2} exhibiting minimum resistivity and (f) 1224 J cm^{-2} exhibiting oversintering. (The error bar represents standard deviation).

gap distance such as 1050 μm the resistivity increase is less pronounced, and it is similar to the resistivity of the same electrodes after sintering at 1020 J cm^{-2} (figures 6(e)–(g)). Also, figure S2 shows the non-normalized resistivity variation of corner and center after sintering at 1020 J cm^{-2} and 1224 J cm^{-2}.

The reason for resistivity variations between individual, corner and center electrodes in arrays after hotplate drying could be different amounts of carbon-based materials (binders, surfactants, ligands, and residual solvent) that remain in the electrodes. In order to study the residual ink after 30 min of drying on a hot plate at 60 °C, x-ray photoelectron spectroscopy (XPS) is used for individual, corner, and center electrodes of a 7 × 7 electrode array with a gap distance of 100 μm. The results are shown in table 1 and confirm that after drying of the electrodes, the residual amount of carbon-based materials is dependent on the position of electrodes in an array, which causes resistivity variations.

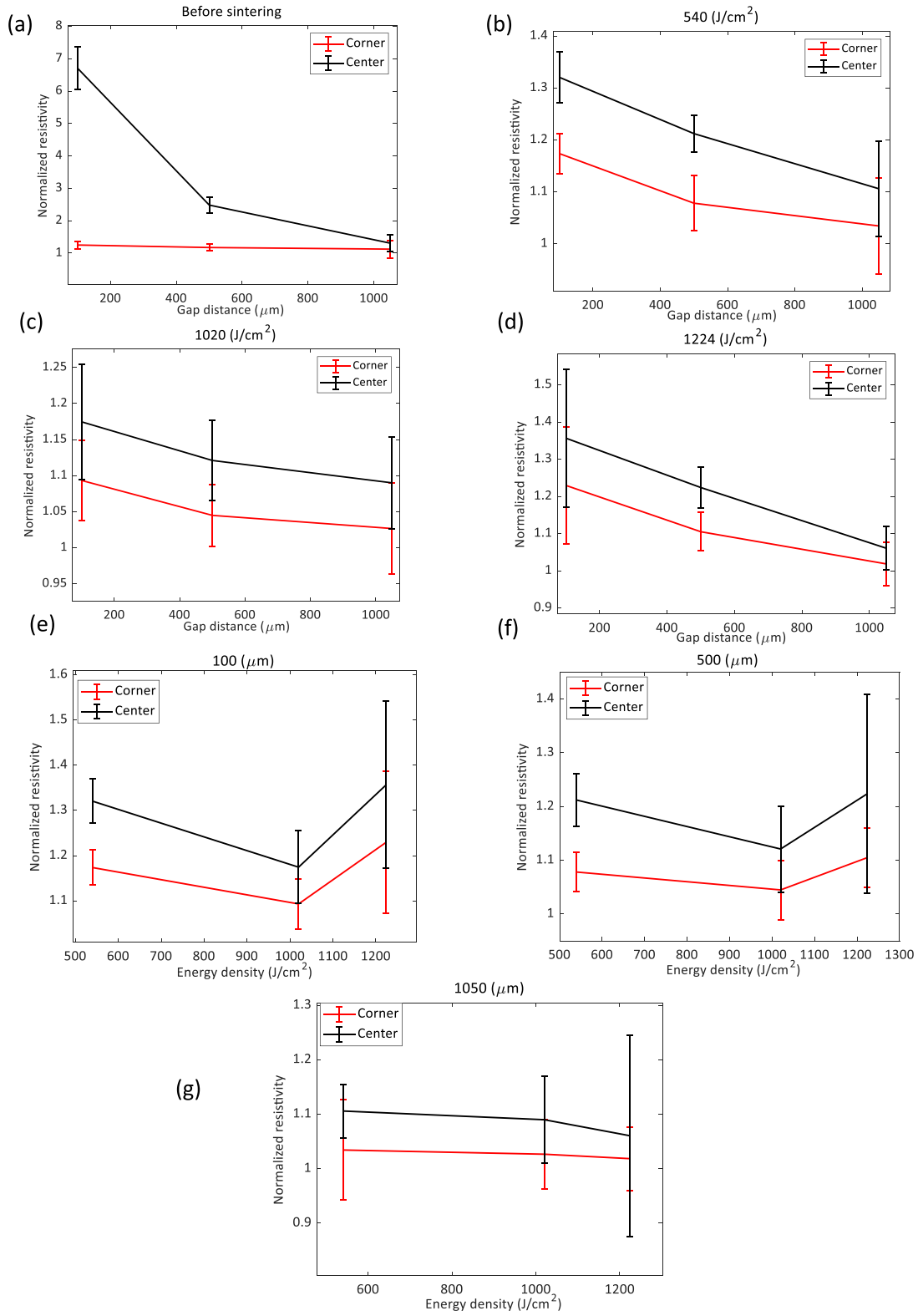

Figure 6. Average resistivity of corner and center electrodes in a 7 × 7 array with three different gap distances normalized to the individual electrode (a) after drying, (b) after IPL sintering at 540 J cm^{-2}, (c) 1020 J cm^{-2}, (d) 1224 J cm^{-2}, and normalized resistivity of corner and center electrodes for different energy densities at a gap distance of (e) 100 μm, (f) 500 μm, and (g) 1050 μm. (The error bar represents standard deviation directly).

SEM images of individual, corner, and center electrodes (figure 7) show the morphology of the printed films after drying and IPL sintering. After drying before sintering, SEM images show individual particles and no significant difference in morphology because particles are not sintered yet. Differences in resistivity can be explained by the differences in carbon content from XPS (table 1). After sintering, the images reveal distinct crack patterns, with fewer cracks in the individual electrodes, more in the corner

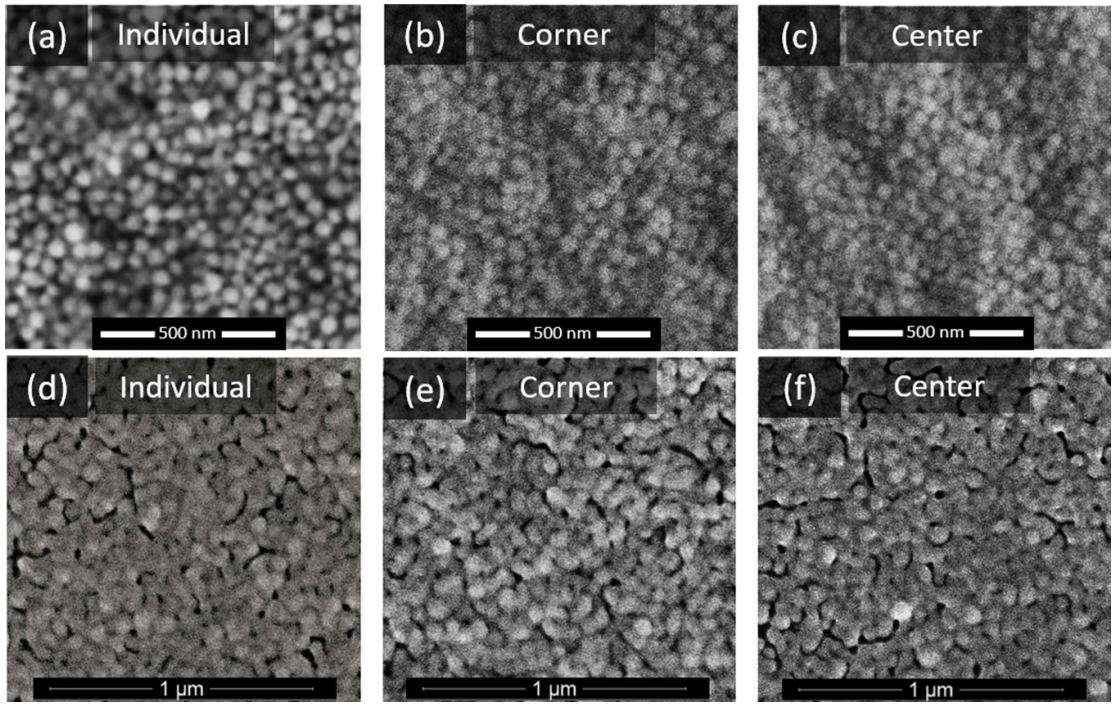

Figure 7. SEM images of (a) individual, (b) corner and (c) center electrodes of a 7 × 7 array after drying at 60 °C for 30 min and after IPL sintering (d), (e), and (f) at 1020 J cm^{-2}.

Table 1. Atomic percentages of dried electrodes from XPS showing more residual ink inside of arrays.

XPS	C1s	Ag3d	S2p	O1s
Electrode Position	Rel.At.%	Rel.At.%	Rel.At.%	Rel.At.%
Individual	33.4	42.6	19.5	4.5
Corner	42.3	35.0	15.3	7.4
Centre	45.5	32.9	13.0	8.7

electrodes, and the highest number of cracks in the center electrodes. These observations align with our XPS analysis, indicating that the presence of cracks correlates with the residual carbon residual content after drying and resistivity.

The thermal processes during IPL sintering were simulated using a time-dependent 3D COMSOL Multiphysics model to the investigate temperature distribution over square shaped silver electrodes on the glass substrate. The size and thickness of electrodes are the same as the experimental samples. Heat transfer from the light source, convection, and surface to ambient radiation are applied to the electrodes. A single pulse with 4.6 J cm^{-2} energy density and 2 ms pulse width is applied to a 3 × 3 electrode array for four different gap distances. The temperature difference between corner and center at 2 ms is around 200 K and it is not dependent on the gap distance. However, after the end of the light pulse during cooling, the temperature gradient is different for different gap distances. At 40 ms, the temperature gradients for arrays with 50 μm, 100 μm, 250 μm, and 500 μm gap distance are 42 K, 37 K, 25 K, and 20 K, respectively (figures 8(a)–(d)). The temperature variation results for 5 × 5 and 7 × 7 electrode arrays with different gap distances are provided in the supplementary information.

This simulation illustrates the temperature distribution over electrode arrays with different gap distances. Printed electrodes with smaller gap distance show a higher resistivity after drying compared to a larger gap distance but the temperature distribution during IPL leads to a higher resistivity reduction factor compared to the larger gap distance. Moreover, the electrodes with smaller gap distance oversinter at a lower energy density compared to the larger gap distance due to the higher temperature difference that also lasts for a longer time for smaller gap distance. The temperature variation is not dependent on the number of electrodes, while it is dependent on the gap distance. For the same gap distance but different number of electrodes, temperature variations are similar. This is also observed experimentally in figures 5(b)–(d) where the lowest resistivity and the resistivity after oversintering are the same for different numbers of electrodes with a constant gap distance.

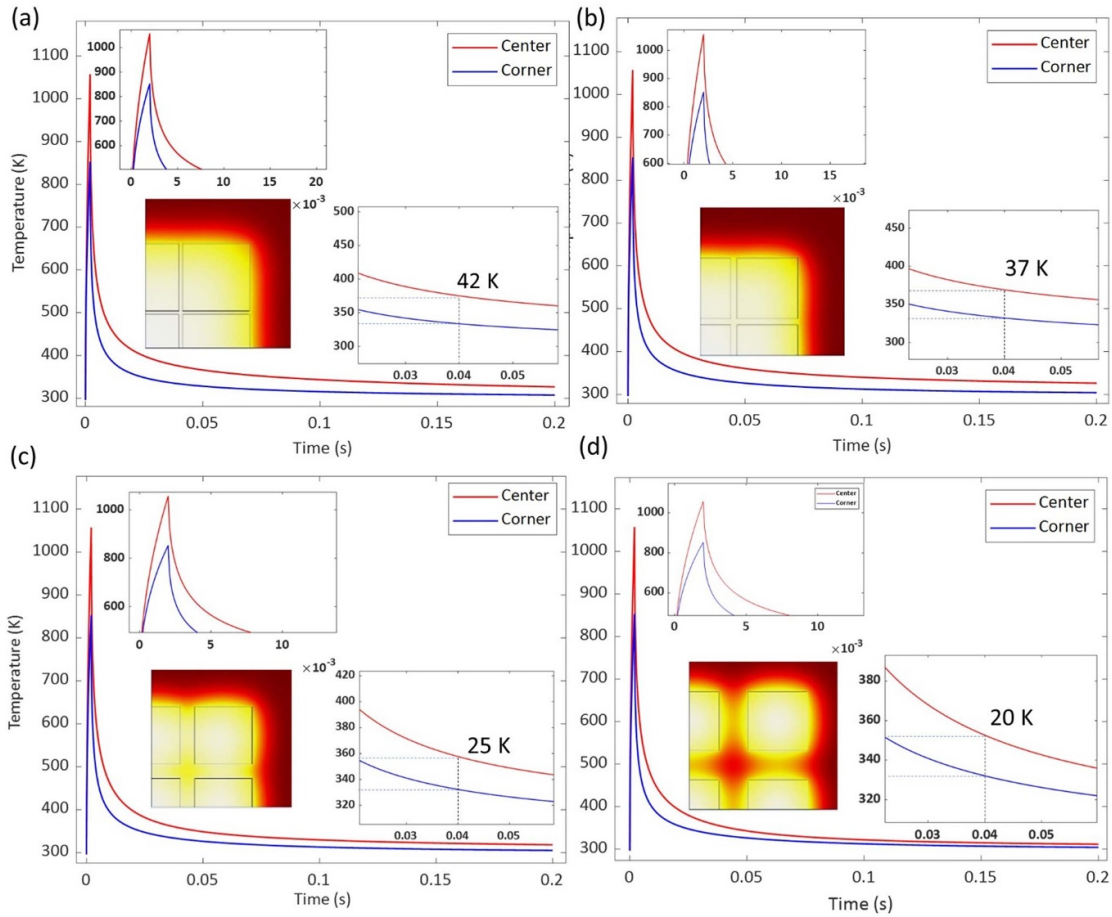

Figure 8. Temperature variation during IPL sintering of a 3 × 3 electrode array with a single pulse of 4.6 J cm^{-2} with (a) 50 μm, (b) 100 μm, (c) 250 μm, and (d) 500 μm gap distance.

This means the gap distance between electrodes plays the most important role, which is shown in figures S3 and S4.

3. Conclusion

In this work, we report the resistivity variation of printed electrodes in different designs, pattern sizes and densities using inkjet printing of metal nanoparticles. The pattern-dependent drying and sintering effects on the resistivity of electrodes are studied. It is shown that for the same drying temperature and duration, the sooner the electrode dries the lower its resistivity will be. Electrode arrays with different numbers of electrodes and gap distances are studied after drying and sintering. Higher number of electrodes and lower gap distance between electrodes result in higher resistivity after drying. We used COMSOL Multiphysics to simulate how temperature changes in electrode arrays during IPL sintering. This helped us study how the design, size, and density of the printed elements affect the temperature. We found that the difference in temperature between the center and the corners of the array depends on the gap distance between them. When this gap is smaller, the reduction in resistivity is more significant compared to arrays with larger gap distances after IPL sintering. The resistivity variation is studied for a number of line patterns with different local geometry density and number of corners but the same volume of ink (number of droplets). The patterns with a higher local pattern density and the same number of corners show a higher resistivity. In addition, after IPL sintering, the patterns with higher local pattern density result in a higher resistivity reduction factor. These effects need to be characterized when developing new printed electronics processes to enable circuit designers to consider the effect of pattern geometry on resistance and circuit performance in their designs. An AI-based predictive model can estimate the resistivity of inkjet-printed designs based on various parameters, including design, drying, and sintering conditions. Future research in this direction could enhance our ability to optimize printed electronics. These insights will empower circuit designers to optimize printed circuits effectively, considering parameters such as feature spacing, shape, gap distances, and sintering settings, ensuring the desired electrical performance in various printed electronic applications and advancing the field of printed electronics. Also, simulating the drying process of inkjet-printed patterns could help to further understand how different designs affect

evaporation rates and vapor pressure. Future work could also study convection drying and the effect of air flow during drying to control resistivity variations. In summary, our study provides practical guidance for optimizing printed circuits. For dense patterns, careful control of feature spacing, especially with IPL power management, is crucial. If there is flexibility in the layout, strategic considerations of shapes and gap distances can be made to optimize electrical performance. Minimizing oversintering is vital for achieving uniform resistivity. For specific resistivity goals, adjusting shape, gap distances, and applying IPL sintering with customized settings are recommended. These insights empower designers to tailor their layouts effectively, ensuring desired electrical performance in diverse printed electronic applications.

4. Materials and methods

4.1. Inkjet printing

A square pattern (1 mm × 1 mm) is printed individually and in arrays of 9, 25, and 49 squares on borosilicate glass substrates (Fisher Scientific) using two different commercial inks: silver nanoparticle ink (ANP DGP 40LT-15 C, Advanced Nano Products, Co., Sejong, Korea) and copper nanoparticle ink (Metalon CI-005, NovaCentrix, Austin, TX). The solvent of the silver and copper nanoparticle inks are TGME and glycol ether respectively. A piezoelectric inkjet nozzle with a diameter of 60 μm (MJ-ATP-01-60-8MX, Microfab Technologies, Inc. Plano, TX) is used in a custom-made inkjet printer. In order to have stable jetting, a trapezoidal bipolar waveform of 60 V peak-to-peak is applied to the nozzle to jet the silver ink with 10–17 mPa.s and copper ink with 13 mPa.s viscosity. The printed copper and silver electrodes are dried in a vacuum oven and on a hot plate at 60 °C, respectively. The square patterns are printed with an inward spiral drop sequence with 120 μm drop spacing for the first boundary, and the rest of the spiral is printed with 65 μm drop spacing. Arrays of 9 (3 × 3), 25 (5 × 5), and 49 (7 × 7) square electrodes are printed with different gap distances. Five more complicated line patterns (line, spiral, small and large U shape and square wave) are printed with a same total number of droplets to study the resistivity variation due to differences in pattern.

4.2. Post-processing by drying and IPL sintering

Printed squares are dried on a hot plate at 60 °C for 20 min to create solid films of metal nanoparticles. The next step is IPL sintering (X-1100, XENON Corporation, Wilmington, MA) with different IPL parameters to control the quality of thin films and yield the lowest electrical resistivity in ambient conditions at room temperature. The IPL parameters directly change the energy density (J.cm^{-2} per pulse). The pulse width of the incident light can be controlled, which will also affect the energy density per pulse. Pulses with energy density between 4.5 J cm^{-2} (2 ms pulse width and 2500 V) and 6.8 J cm^{-2} (3 ms pulse width and 3000 V) are applied to the printed squares with different numbers of pulses (5–180). The samples are placed at a distance of 2.5 cm from the light source.

4.3. Characterization

The electrical resistivity is measured using a probe station connected to a semiconductor parameter analyzer (Keithley 4200A). Four probe needles touch the corners of an individual square, and the sheet resistance of the thin film will be calculated by the VDP method. Two of the needles will have a swept current applied, and the other two will record the voltages. Four resistances will be calculated from these measurements with four different probe configurations called R_1, R_2, R_3, and R_4; and the experimental sheet resistance of the square shaped sample ($R_{s,exp}$) can be calculated after R_1, R_2, R_3, and R_4 measurements using equation (2). In our case, as the sample is thin compared to its lateral dimensions, needles are placed at the corners of the square, the surface is homogeneous, and there are no holes in it, R_1, R_2, R_3, and R_4 are equal, and equation (2) can be simplified as equation (3) [47]

$$\exp\left(-\frac{\pi R_1 + R_3}{2R_{s,exp}}\right) + \exp\left(-\frac{\pi R_2 + R_4}{2R_{s,exp}}\right) = 1 \quad (2)$$

$$R_{s,exp} = \frac{\pi}{\ln(2)}\frac{V}{I}. \quad (3)$$

The electrical resistivity is calculated with the thickness of the printed thin film measured using a stylus profilometer (Alpha-Step, D-600, KLA-Tencor, Milpitas, CA). For the resistance measurement of the complex designs, a two-point probe measurement is used by applying voltage and recording current using the same semiconductor parameter analyzer (Keithley 4200A). Also, the error bar represents the standard deviation of multiple measurements from five different samples for each condition. Resistance of different line patterns is converted into resistivity using a COMSOL Multiphysics model. Microscope images of the different printed patterns are imported into COMSOL with the average thickness of each pattern obtained from profilometry. The model is solved to obtain current and voltage distributions for unit resistivity. The experimental resistivity is obtained by dividing the experimental resistance by the simulated resistance. Scanning electron microscopy (SEM) is performed with a field emission SEM (FEG-SEM, Fisher Quanta 3D) to take images of the printed thin films before sintering, after sintering, and after oversintering. XPS measurements are performed using a K-alpha x-ray photoelectron spectrometer (Escalab 250Xi, Thermo Fisher Scientific, East Grinstead, UK). The survey spectra are taken with 1 eV step size and

a 100 eV pass energy. Elemental spectra are recorded with 0.1 eV step size and a pass energy of 20 eV.

4.4. Simulation

The thermal processes during IPL sintering are simulated to gain more insights into the heat and temperature distribution over the printed electrodes on the glass substrate. A time-dependent 3D COMSOL Multiphysics model is created based on the built-in heat transfer models. The model simulates the heat distribution of the IPL on the silver electrodes and solves the heat transfer equation for three main boundary conditions. General inward heat flux on the top surface of electrodes is used to simulate the energy density of IPL sintering. Convective cooling heat flux is applied for both electrodes and glass substrate. Surface to ambient radiation is only used for electrodes. The pulse width and energy density are chosen based on experiments, and a 2 ms pulse with 4.6 J.cm^{-2} is applied to the 9 (3×3), 25 (5×5), and 49 (7×7) electrode arrays. Only a quarter of each array is simulated using symmetry to reduce the computational volume.

Data availability statement

The data that support the findings of this study are openly available at the following URL/DOI: [https://borealisdata.ca/privateurl.xhtml?token=d67637d7-5388-4980-84f3-d7759d0eda1c].

Acknowledgments

We acknowledge the support of the Natural Sciences and Engineering Research Council of Canada (NSERC), funding reference number STPGP 521480-18. The XPS data was collected at the University of Toronto's Ontario Centre for the Characterization of Advanced Materials (OCCAM). SEM images were taken at the Advanced Light and Electron Microscopy Facility at York University. We also acknowledge CMC Microsystems for providing the COMSOL software license.

Conflict of interest

The Authors declare no Competing Financial or Non-Financial Interests

Author contributions

Milad Ghalamboran: Conceptualization, methodology, investigation, analysis, simulation, data curation, visualization, writing original draft. Mohammad Nazeri: Investigation, editing. Gerd Grau: Supervision, validation, writing, review and editing, funding acquisition, resources, conceptualization.

ORCID iDs

Milad Ghalamboran https://orcid.org/0000-0002-0070-0563
Gerd Grau https://orcid.org/0000-0001-5729-9160

References

[1] Tong C 2022 Printed flexible organic light-emitting diodes *Advanced Materials for Printed Flexible Electronics* (Springer) pp 347–99
[2] Cao M, Hyun W J, Francis L F and Frisbie C D 2020 Inkjet-printed, self-aligned organic Schottky diodes on imprinted plastic substrates *Flex. Print. Electron.* **5** 015006
[3] Worsley R *et al* 2018 All-2D material inkjet-printed capacitors: toward fully printed integrated circuits *ACS Nano* **13** 54–60
[4] Ju B, Kim I, Li B M, Knowles C G, Mills A, Grace L and Jur J S 2021 Inkjet printed textile force sensitive resistors for wearable and healthcare devices *Adv. Healthcare Mater.* **10** 2100893
[5] Cao M, Jochem K, Hyun W J, Francis L F and Frisbie C D 2018 Self-aligned inkjet printing of resistors and low-pass resistor–capacitor filters on roll-to-roll imprinted plastics with resistances ranging from 10 to 106 Ω *Flex. Print. Electron.* **3** 045003
[6] Karunakaran S K, Arumugam G M, Yang W, Ge S, Khan S N, Lin X and Yang G 2019 Recent progress in inkjet-printed solar cells *J. Mater. Chem.* A **7** 13873–902
[7] Mathies F, Eggers H, Richards B S, Hernandez-Sosa G, Lemmer U and Paetzold U W 2018 Inkjet-printed triple cation perovskite solar cells *ACS Appl. Energy Mater.* **1** 1834–9
[8] Trudeau C, Beaupré P, Bolduc M and Cloutier S G 2020 All inkjet-printed perovskite-based bolometers *npj Flex. Electron.* **4** 34
[9] Ruiz-Preciado L A, Baek S, Strobel N, Xia K, Seiberlich M, Park S-M, Lemmer U, Jung S and Hernandez-Sosa G 2023 Monolithically printed all-organic flexible photosensor active matrix *npj Flex. Electron.* **7** 6
[10] Clement B, Lyu M, Sandeep Kulkarni E, Lin T, Hu Y, Lockett V, Greig C and Wang L 2022 Recent advances in printed thin-film batteries *Engineering* **13** 238–61
[11] Abutarboush H F 2022 Silver nanoparticle inkjet-printed multiband antenna on synthetic paper material for flexible devices *Alexandria Eng. J.* **61** 6349–55
[12] Shastri A, Sanz-Izquierdo B and Gao S 2022 Manufacturing considerations for the development of reconfigurable antennas using inexpensive inkjet printing *IEEE Trans. Compon. Packag. Manuf. Technol.* **12** 1021–8
[13] Divya M, Pradhan J R, Priyadarsini S S and Dasgupta S 2022 High operation frequency and strain tolerance of fully printed oxide thin film transistors and circuits on PET substrates *Small* **18** 2202891
[14] Naderi P and Grau G 2022 Organic thin-film transistors with inkjet-printed electrodes on hydrophobic Teflon-AF gate dielectric with reversible surface properties *Org. Electron.* **108** 106612
[15] Grau G and Subramanian V 2016 Fully high-speed gravure printed, low-variability, high-performance organic polymer transistors with sub-5 V operation *Adv. Electron. Mater.* **2** 1500328
[16] Bonnassieux Y *et al* 2021 The 2021 flexible and printed electronics roadmap *Flex. Print. Electron.* **6** 023001
[17] Wu W 2022 *Printed Electronics Technologies* (Royal Society of Chemistry)
[18] Sirringhaus H and Shimoda T 2003 Inkjet printing of functional materials *MRS Bull.* **28** 802–6
[19] Wang X, Zhang M, Zhang L, Xu J, Xiao X and Zhang X 2022 Inkjet-printed flexible sensors: from function materials,

manufacture process, and applications perspective *Mater. Today Commun.* **31** 103263
[20] Abdolmaleki H, Kidmose P and Agarwala S 2021 Droplet-based techniques for printing of functional inks for flexible physical sensors *Adv. Mater.* **33** 2006792
[21] Kamyshny A and Magdassi S 2014 Conductive nanomaterials for printed electronics *Small* **10** 3515–35
[22] Wang Y H, Du D X, Xie H, Zhang X B, Lin K W, Wang K and Fu E 2021 Printability and electrical conductivity of silver nanoparticle-based conductive inks for inkjet printing *J. Mater. Sci. Mater. Electron.* **32** 496–508
[23] Shahariar H, Kim I, Soewardiman H and Jur J S 2019 Inkjet printing of reactive silver ink on textiles *ACS Appl. Mater. Interfaces* **11** 6208–16
[24] Zhao D, Zhou H, Wang Y, Yin J and Huang Y 2021 Drop-on-demand (DOD) inkjet dynamics of printing viscoelastic conductive ink *Addit. Manuf.* **48** 102451
[25] Jia L-C, Zhou C-G, Sun W-J, Xu L, Yan D-X and Li Z-M 2020 Water-based conductive ink for highly efficient electromagnetic interference shielding coating *Chem. Eng. J.* **384** 123368
[26] Ibrahim N, Akindoyo J O and Mariatti M 2022 Recent development in silver-based ink for flexible electronics *J. Sci. Adv. Mater. Devices* **7** 100395
[27] Ferrari L M, Ismailov U, Badier J-M, Greco F and Ismailova E 2020 Conducting polymer tattoo electrodes in clinical electro- and magneto-encephalography *npj Flex. Electron.* **4** 4
[28] Kelly A G *et al* 2022 Highly conductive networks of silver nanosheets *Small* **18** 2105996
[29] Yaniv Z 2009 *Nanotechnology and its Contribution to Technical Inks for Printed Electronics* (Appl. Nanotech, Inc., USA, Euro Disp) pp 1–4
[30] Kordás K, Mustonen T, Tóth G, Jantunen H, Lajunen M, Soldano C, Talapatra S, Kar S, Vajtai R and Ajayan P 2006 Inkjet printing of electrically conductive patterns of carbon nanotubes *Small* **2** 1021–5
[31] Wiklund J *et al* 2021 A review on printed electronics: fabrication methods, inks, substrates, applications and environmental impacts *J. Manuf. Mater. Process.* **5** 89
[32] Perelaer J, Smith P J, Mager D, Soltman D, Volkman S K, Subramanian V, Korvink J G and Schubert U S 2010 Printed electronics: the challenges involved in printing devices, interconnects, and contacts based on inorganic materials *J. Mater. Chem.* **20** 8446–53
[33] Bhat K S, Ahmad R, Wang Y and Hahn Y-B 2016 Low-temperature sintering of highly conductive silver ink for flexible electronics *J. Mater. Chem.* C **4** 8522–7
[34] Deegan R D, Bakajin O, Dupont T F, Huber G, Nagel S R and Witten T A 1997 Capillary flow as the cause of ring stains from dried liquid drops *Nature* **389** 827–9
[35] Fischer B J 2002 Particle convection in an evaporating colloidal droplet *Langmuir* **18** 60–67
[36] Wünscher S, Abbel R, Perelaer J and Schubert U S 2014 Progress of alternative sintering approaches of inkjet-printed metal inks and their application for manufacturing of flexible electronic devices *J. Mater. Chem.* C **2** 10232–61
[37] Jang S and Rahman M 2021 Effect of sintering atmospheres on printed silver nanoparticle patterns for flexible electronics application *Appl. Phys.* A **127** 1–14
[38] Schroder K, McCool S and Furlan W 2006 Broadcast photonic curing of metallic nanoparticle films *NSTI Nanotech. May* **7** 11
[39] Kamyshny A, Steinke J and Magdassi S 2011 Metal-based inkjet inks for printed electronics *Open Appl. Phys. J.* **4** 19–36
[40] Kinney L C and Tompkins E H 1969 Method of making printed circuits *US Patent* US3451813A
[41] Abbel R, van Lammeren T, Hendriks R, Ploegmakers J, Rubingh E J, Meinders E R and Groen W A 2012 Photonic flash sintering of silver nanoparticle inks: a fast and convenient method for the preparation of highly conductive structures on foil *MRS Commun.* **2** 145–50
[42] Chen W, Xiao D, Xiao H, Wang X, Peng W and Zhang H 2022 Inkjet-printed radiation pattern reconfigurable receiving antenna for 2.45 GHz wireless power transfer application *AIP Adv.* **12** 025023
[43] Langwieser R *et al* 2022 Silver ink printed logarithmic spiral antenna *2022 45th Int. Spring Seminar on Electronics Technology (ISSE)* (IEEE) pp 1–7
[44] Barbalace G, Natali D and Scolari M 2022 Manufacturing of silver-ink micrometer inductors through multilayer DOD printing for VHF power transfer *2022 17th Conf. on Ph. D Research in Microelectronics and Electronics (PRIME)* (IEEE) pp 25–28
[45] Jang Y-R, Ryu C-H, Hwang Y-T and Kim H-S 2021 Optimization of intense pulsed light sintering considering dimensions of printed Cu nano/micro-paste patterns for printed electronics *Int. J. Precis. Eng. Manuf. Technol.* **8** 471–85
[46] Khilifi D, Foudhil W, Fahem K, Harmand S and Ben J S 2019 Study of the phenomenon of the interaction between sessile drops during evaporation *Therm. Sci.* **23** 1105–14
[47] Reveil M, Sorg V C, Cheng E R, Ezzyat T, Clancy P and Thompson M O 2017 Finite element and analytical solutions for van der Pauw and four-point probe correction factors when multiple non-ideal measurement conditions coexist *Rev. Sci. Instrum.* **88** 94704